

# Analysis of $\text{PF}_6^-$ Anion Intercalation/De-Intercalation Mechanisms in Graphite Cathodes of Sodium Dual-Ion Batteries

Ignacio Cameán,\*<sup>[a]</sup> Belén Lobato,<sup>[a]</sup> Nuria Cuesta,<sup>[a]</sup> and Ana B. García<sup>[a]</sup>

A detailed study of the intercalation/de-intercalation mechanisms of  $\text{PF}_6^-$  anions in a graphite cathode of sodium dual-ion batteries is carried out by cyclic voltammetry. The influence of the continuous anion intercalation/de-intercalation on the graphite structure is investigated by ex-situ XRD after cycling. It was concluded that the intercalation/de-intercalation occurs through a combination of diffusion-controlled and pseudocapacitive mechanisms. Initially, the contribution of the diffusion-controlled is significant, specifically at the highest voltage and at the lowest scan rates which agrees with the slow kinetic of this mechanism and its usual prevalence in carbon materials with a graphitic structure. However, the continuous anion

intercalation/de-intercalation causes some deterioration of the graphite structural order, even from the initial cycles, as it was demonstrated by the evolution of the crystalline parameters, interlayer spacing,  $d_{002}$ , and crystallite size,  $L_c$ . This deterioration hinders the diffusion-controlled anion intercalation/de-intercalation and, as a consequence, the pseudocapacitive becomes the main mechanism along cycling. Therefore, since graphite is capable of intercalating  $\text{PF}_6^-$  anions at high voltages through a capacitive mechanism, with its consequent rapid kinetics, this carbon material is an excellent candidate for using as cathode in high power sodium dual-ion batteries, in which, kinetically fast mechanisms are required.

## Introduction

Currently, lithium-ion batteries (LIBs) hold the first position in the battery market because of their excellent performance mainly in terms of energy. Nevertheless, for application in the storage of the renewable energy, LIBs have an important disadvantage on account of their relatively high energy cost (at least  $220 \text{ } \text{S kWh}^{-1}$ ) which is mainly due to the lithium compounds used as both cathode active material and electrolyte salt. For this application, i.e., gigawatt-scale, the energy cost is the most important issue, whereas the energy of the battery is not such as critical factor.<sup>[1]</sup> In this context, dual-ion batteries (DIBs) are attracting great scientific interest in last years as an alternative to LIBs because of their (i) expected lower energy cost since the lithium-based compounds of the cathode are here replaced by carbon materials, which can be produced from a wide range of precursors and are characterized by their low-cost, availability, and properties that can be easily fixed to specific uses, and (ii) higher operating voltage.<sup>[1–8]</sup> The DIBs operation is based on the intercalation of both cations and anions from the electrolyte salt in the active material of the anode and the cathode, respectively, during the charge process

while electrons flow from the positive to the negative electrode through an external circuit to balance the charge. The reverse process occurs in the discharge. Therefore, the electrolyte plays a crucial role in the operation of DIBs. Lithium salt-based and more recently, sodium salt-based electrolytes have been studied for these batteries, therefore denoted Li-DIBs and Na-DIBs, respectively.<sup>[2,10–14]</sup> Among them, Na-DIBs combine the benefits of using carbon materials in both electrodes and sodium-based compounds, which are of greater abundance, lower cost and more environmentally-friendly nature than the lithium compounds.

Regarding to Na-DIBs electrode materials, oil-derived synthetic graphite,<sup>[3,9,10,15]</sup> and other carbon materials<sup>[16–23]</sup> such as biogas-derived nanofibers,<sup>[16]</sup> amorphous mesoporous carbon,<sup>[17]</sup> expanded graphite<sup>[18]</sup> and graphitized carbon xerogel<sup>[23]</sup> have recently investigated as cathodes for the intercalation of several anions, i.e.,  $\text{BF}_4^-$ ,  $\text{ClO}_4^-$  and mainly  $\text{PF}_6^-$ , from the corresponding sodium salt dissolved in mixtures of organic carbonates, such as ethylene carbonate (EC), ethyl methyl carbonate (EMC), dimethyl carbonate (DMC), diethyl carbonate (DEC). Among them, graphite cathode and  $\text{PF}_6^-$  anion clearly outperformed the others.<sup>[10,15,24–25]</sup>

The electric current response from ion intercalation into graphite can be due to a diffusion-controlled faradaic process or produced by a capacitive process.<sup>[26]</sup> In relation to the latter, the pseudocapacitance concept was first described by Trassati and Buzzanca in 1971 in a study on  $\text{RuO}_2$  electrodes.<sup>[27]</sup> This concept refers to the electrochemical capacitance that involves faradaic charge-transfer reactions. Subsequently, Conway identified faradaic mechanisms that can give rise to capacitive responses.<sup>[26]</sup> One of this mechanism is the intercalation pseudocapacitance (or pseudo-capacitive intercalation), which is ascribed to ion intercalation into tunnels or layers of the

[a] Dr. I. Cameán, Dr. B. Lobato, Dr. N. Cuesta, Dr. A. B. García  
Instituto de Ciencia y Tecnología del Carbono, INCAR-CSIC  
Francisco Pintado Fe 26, 33011, Oviedo (Spain)  
E-mail: icamean@incar.csic.es

 Supporting information for this article is available on the WWW under <https://doi.org/10.1002/batt.202300508>

 © 2023 The Authors. *Batteries & Supercaps* published by Wiley-VCH GmbH. This is an open access article under the terms of the Creative Commons Attribution Non-Commercial NoDerivs License, which permits use and distribution in any medium, provided the original work is properly cited, the use is non-commercial and no modifications or adaptations are made.

active material accompanied by a faradaic charge-transfer without crystalline phase change.<sup>[27]</sup> According to Brezesinski et al.,<sup>[30]</sup> the capacitive storage could have two different features: electric double-layer capacitive and/or pseudocapacitive. The latter arises from reversible redox reactions near the electrode surface (redox capacitance) or ion intercalation into open channel or van der Waals gaps of crystalline material (pseudocapacitive intercalation). Considering the absence of surface functional groups in graphite as well as its low surface area, the capacity from capacitive phenomena of graphite electrodes was associated with a pseudo-capacitive intercalation (PCI).<sup>[29,31]</sup> This kind of intercalation, which unlike diffusion-controlled intercalation (DCI) involves fast kinetics, could be related to the following graphite characteristics: (i) well-defined layered structure that allows the charge storage, (ii) high electrical conductivity that facilitates the electron transport and (iii) the decrease in the reactivity of the ions due to the coordination by solvent molecules encouraging the charge adsorption between the graphene sheets instead of forming bonds with the carbon atoms.

The contributions of DCI and PCI to the measured graphite electrode current response can be determined by both qualitative and quantitative analysis of cyclic voltammetry at different scan rates. For qualitative analysis, the power law relationship between the current intensity  $i$  (A) and the scan rate  $v$  ( $\text{mVs}^{-1}$ ) at a given potential through the  $i = av^b$  equation is used. In this equation,  $a$  and  $b$  are adjustable parameters.<sup>[32]</sup> The value of the  $b$  parameter (in the interval 0.5–1.0) determines the contribution of the two intercalation mechanisms with 0.5 indicating that the current comes primarily from DCI, whereas for 1.0 the current is predominantly from PCI. Regarding the quantitative analysis, the method proposed by Dunn et al. is widely applied today.<sup>[33]</sup> Thus, the contribution of both intercalation processes can be estimated by  $i = k_1v + k_2v^{1/2}$  equation where  $i$  (A) is the current intensity at a given potential,  $v$  ( $\text{mVs}^{-1}$ ) is the corresponding scan rate, and  $k_1$  and  $k_2$  are constants. In this equation,  $k_1v$  and  $k_2v^{1/2}$  correspond to the contributions of DCI and PCI currents, respectively. Following this methodology, kinetic analysis of the intercalation of  $\text{PF}_6^-$  anions into graphite electrodes, from both lithium salt- and sodium salt-based electrolytes have been recently carried out.<sup>[3,11,21,22,26,34]</sup> In general, it was concluded that the PCI contribution is relevant, thus explaining the excellent rate performance of these electrodes. In this context, Y. Wang et al. studied the effect of the addition of fluoroethylene carbonate (FEC) to a 3 M  $\text{LiPF}_6$  in EMC electrolyte on  $\text{PF}_6^-$  anion intercalation mechanism. They found that the  $b$  parameter value increased from 0.82–0.96 (mostly capacitive process with a small contribution of DCI) to close to 1.00, suggesting that the presence of FEC favored the capacitive intercalation process, i.e., faster anion intercalation/de-intercalation into graphite electrode.<sup>[34]</sup> The kinetic study of Fen et al. also revealed that a significant proportion of the anion ( $\text{PF}_6^-$  from 2 M  $\text{LiPF}_6$  in EMC) intercalation into a graphite electrode came from a capacitive process. In addition, the PCI quantitative contribution to the total electrode capacity increased remarkably by increasing the scan rate. Thus, PCI values of 75 % and 95 % at scan rates of 0.1

and 1.0  $\text{mVs}^{-1}$ , respectively, were calculated. On the other hand, this study also showed that unlike anion, the  $\text{Li}^+$  cation intercalation into a graphite electrode is a totally diffusion-controlled process with  $b$  values of 0.52 at very low scan rates (0.02–0.05  $\text{mVs}^{-1}$ ).<sup>[26]</sup>

In this work, a detailed and exhaustive study of the intercalation (pseudo-capacitive and diffusion-controlled) of  $\text{PF}_6^-$  anions, from a sodium salt-based electrolyte, in a graphite electrode of a dual-ion battery is carried out. In addition, the de-intercalation mechanisms were also studied. As a great novelty to previous works in this field, the evolution of these intercalation/de-intercalation mechanisms and of their respective quantitative contributions to electrode capacity (charge/discharge) during prolonged cycling is investigated for the first time. Specifically, cyclic voltammograms in the 2.9–5.0 V vs. Na/Na<sup>+</sup> potential range obtained at different scan rates (0.2, 0.5, 1.0 and 3.0  $\text{mVs}^{-1}$ ) during 300 cycles are qualitative and quantitative analyzed by applying the  $i = a v^b$  and the  $i = k_1v + k_2v^{1/2}$  equations, respectively, already described above. In addition, the influence of the continuous anion intercalation/de-intercalation on the graphite-like structure of the electrode active material was studied by ex-situ XRD measurements after 20 and 300 cyclic voltammetries at the different scan rates.

## Results and Discussion

### Qualitative analysis of $\text{PF}_6^-$ anion intercalation/de-intercalation mechanisms

Figure 1 shows the voltammograms at 0.2, 0.5, 1.0 and 3.0  $\text{mVs}^{-1}$  scan rates of graphite cathode in 2MNaPF<sub>6</sub>/EC:EMC electrolyte for cycles 20, 50, 100, 200 and 300. In all of them, five anodic peaks (denoted from 1 to 5) at ~4.3 V (1), ~4.5 V (2), ~4.6 V (3), ~4.7 V (4) and ~4.9 V (5), and two cathodic peaks (denoted as 1' and 2') at ~4.1 V (1') and ~4.6 V (2') that correspond to the intercalation/de-intercalation stages of  $\text{PF}_6^-$  anions into/from graphite are observed. This staged mechanism has been reported in previous works for the intercalation of these anions in graphite and/or graphitic materials from sodium salts in different organic carbonate mixtures.<sup>[6,10,23,35]</sup>

As mentioned in the introduction, through the qualitative analysis of these cyclic voltammetries (CVs), i.e., calculating the  $b$  value, the evolution during cycling of diffusion-controlled and pseudo-capacitive intercalation/de-intercalation contributions to the total measured current can be determined. Thus,  $b$  parameter values of all anodic and cathodic peaks of the voltammograms for cycles 20, 50, 100, 200 and 300 were determined by plotting the corresponding  $\log i$  versus  $\log v$  at the different scan rates studied from the CVs in Figure 1. These plots, in which  $b$  corresponds to the slope of the linear correlations ( $R^2$  values mostly  $\geq 0.99$ ) obtained, appear in Figure S1 of the Supporting Information (SI). The calculated  $b$  values, which are in the ranges of 0.88–1.00 (peak 1), 0.79–0.97 (peak 2), 0.83–1.00 (peak 3), 0.92–0.99 (peak 4) and 0.68–0.85 (peak 5), are given in Table S1 (see SI) and their evolution during cycling is shown in Figure 2. In view of these results, it

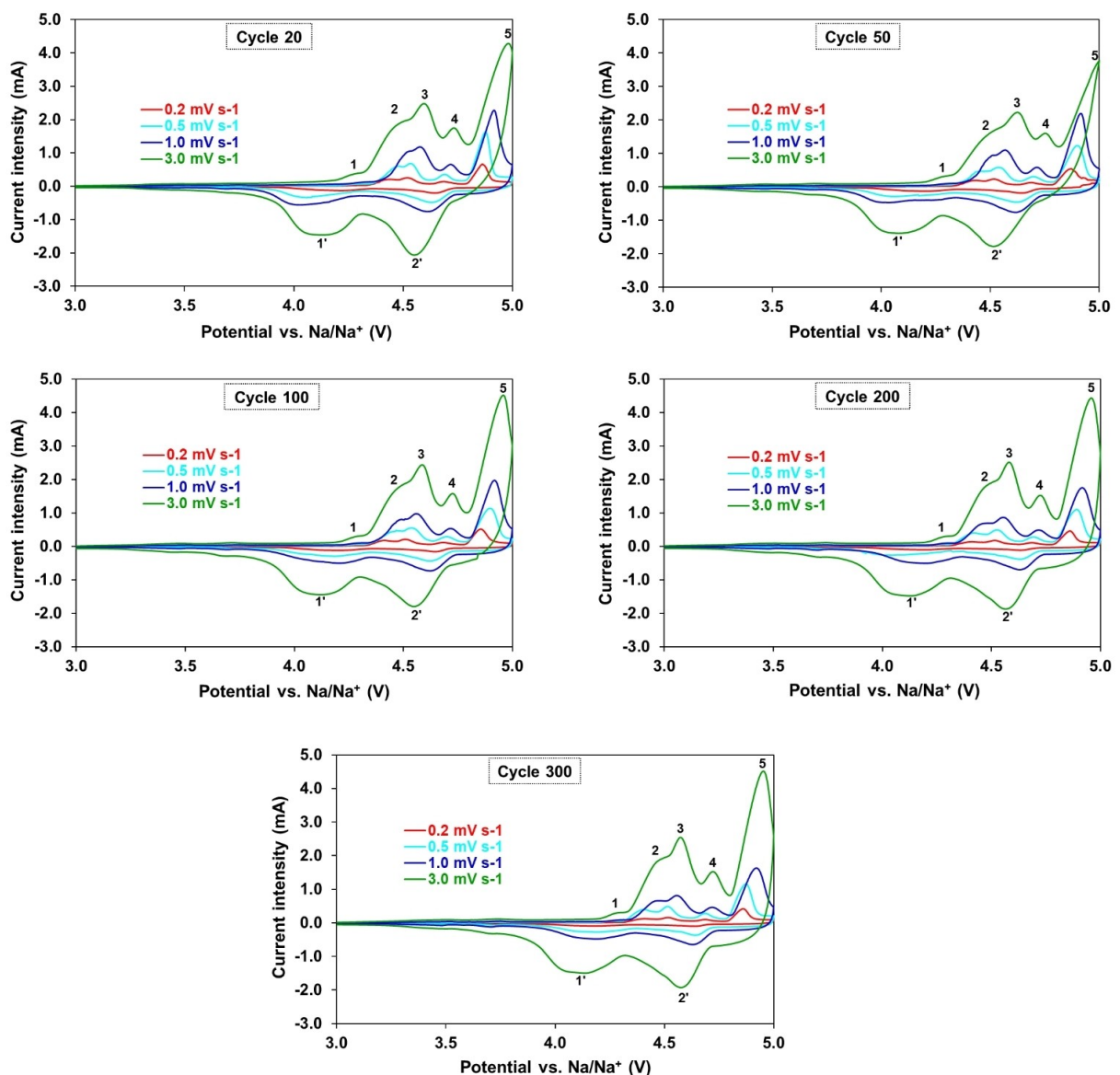


Figure 1. Cyclic voltammograms at scan rates from 0.2 to 3.0 mV s<sup>-1</sup> of graphite cathode in 2MNaPF<sub>6</sub>/EC:EMC electrolyte for cycles 20, 50, 100, 200 and 300.

can be concluded that for the anodic peaks: (i) the *b* values are closer to 1 than to 0.5, i.e. PCI is predominant, (ii) the *b* values tend to increase with cycling, i.e. the predominance of the PCI become greater and (iii) the lowest *b* values were calculated for peak 5, i.e. the greatest contribution of DCI occurs at ~4.9 V. Regarding de-intercalation, Figure S2 (see Supporting Information) shows log *i* vs. log  $\nu$  linear plots ( $R^2 \geq 0.99$ ) for the cathodic peaks (1' and 2') in cycles 20, 50, 100, 200 and 300. As for the intercalation process, pseudo-capacitive de-intercalation (PCDI) is predominant since the two cathodic peak *b* values are in the ranges of 0.88–1.02 (peak 1') and 0.84–1.08 (peak 2') (Table S1 in Supporting Information), and this predominance is more evident with cycling as it can be seen in Figure 3. Furthermore, in cycle 300 the whole discharge capacity is due to PCDI (*b* values ~1).

#### Quantitative analysis of PF<sub>6</sub><sup>-</sup> anion intercalation/de-intercalation mechanisms

As mentioned in the introduction, the quantitative contributions of diffusion-controlled ( $k_1\nu$ ) and pseudocapacitive ( $k_2\nu^{1/2}$ ) intercalations of CV peaks can be calculated by plotting the terms  $i\nu^{-1/2}$  versus  $\nu^{1/2}$  of the Dunn equation<sup>[33]</sup> in the form of  $i\nu^{-1/2} = k_1\nu^{1/2} + k_2$  in which  $k_1$  and  $k_2$  are the slope and the y axis intercept point of the straight line obtained. These plots for the anodic and cathodic peaks from the CVs (Figure 1) in cycles 20, 50, 100, 200 and 300 are given in Figures S3 and S4 (see Supporting Information). Mostly, good linear correlations ( $R^2 > 0.9$ ) were achieved for the peaks along cycling. In addition to the voltage, the contribution percentages of the DCI/DCDI and PCI/PCDI currents to the total measured *i* current for the intercalation/de-intercalation peaks, at the different scan rates and cycles are given in Tables S2–S5 of the Supporting

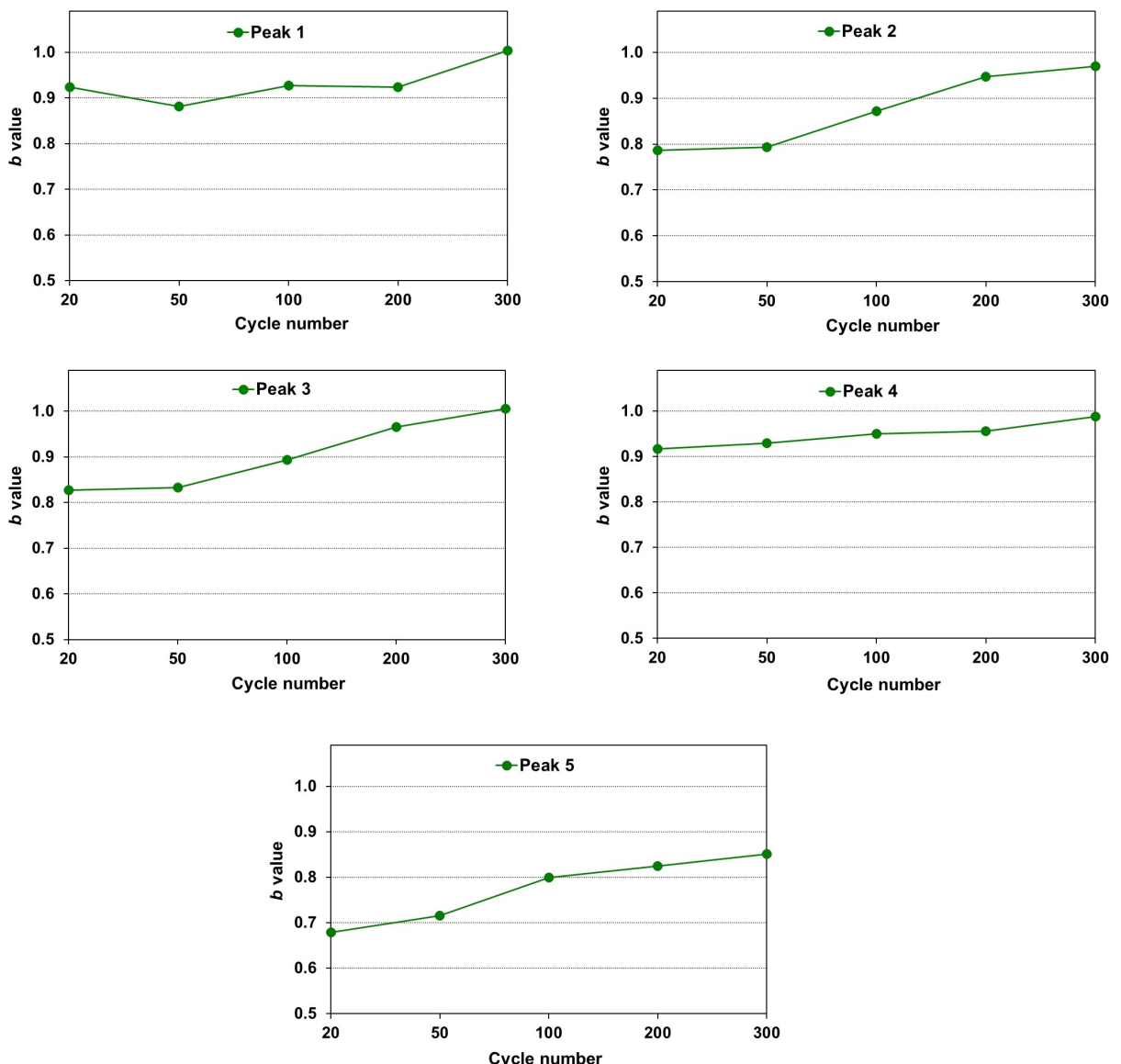


Figure 2. Variation of  $b$  value with cycling for the anodic peaks (1 to 5) of graphite cathode in  $2\text{MNaPF}_6/\text{EC:EMC}$  electrolyte.

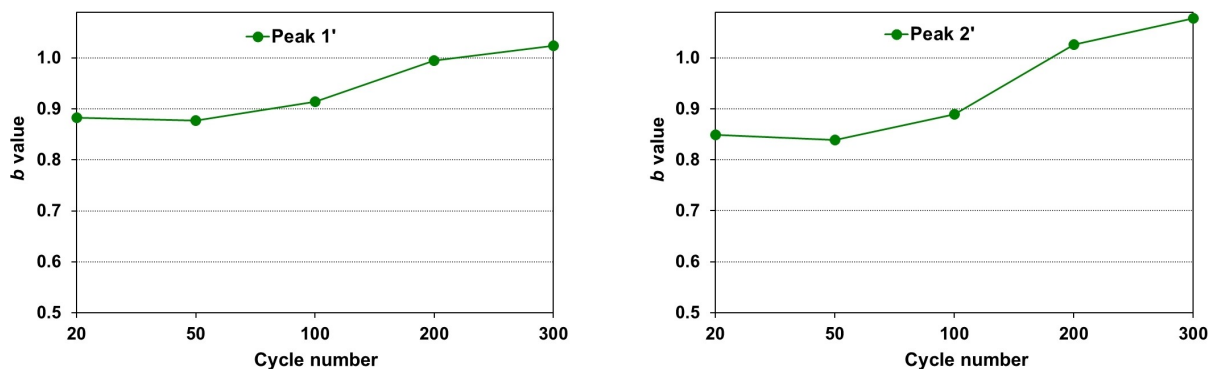


Figure 3. Variation of  $b$  value with cycling for the cathodic peaks (1', 2') of graphite cathode in  $2\text{MNaPF}_6/\text{EC:EMC}$  electrolyte.

Information. These percentages are consistent with the  $b$  values obtained in the qualitative analysis (Table S1). Thus, for

example, the PCDI contribution for the 2' peak at cycle 300 is 100% at all scan rates which was expected considering that the

*b* value calculated for this peak was 1. On the other hand, peak 5 shows the greatest DCI contribution, in the ranges of 48–85, 37–78, 29–71 and 19–49% at 0.2, 0.5, 1.0 and 3.0 mVs<sup>-1</sup>, respectively (Tables S2–S5), which agrees with the lowest *b* value obtained for this peak (Table S1). Accordingly, the total capacity contributions (%) of DCI/DCDI and PCI/PCDI mechanisms to the graphite electrode charge and discharge capacities (values obtained from the cyclic voltammetries), respectively, along cycling for each scan rate were calculated from the integration of the corresponding voltammogram curve (Figure 1) considering the percentage of the process for each peak (Tables S2–S5). These contributions for the PF<sub>6</sub><sup>-</sup> anion intercalation (charge capacity) are given in Figure 4(a). In all cases, for a given cycle, a decrease of the DCI contribution percentages with increasing scan rate is observed. Thus, for example, in cycle 20 these contributions are 66 and 38% of the measured charge capacities at 0.2 and 3.0 mVs<sup>-1</sup>, respectively. This is somehow expected since DCI is a very slow kinetic process. In addition, the percentage of capacity due to this type of intercalation tends to decrease with cycling, independently of the scan rate considered. Moreover, the scope of this decrease goes parallel to the scan rate with losses of 59%, 66%, 70% and 74% from cycles 20 to 300 at 0.2, 0.5, 1.0 and 3.0 mVs<sup>-1</sup>, respectively. Correspondingly, the contributions of PCI to the charge capacity increases with both the cycling and the scan

rate (Figure 4b). In addition, unlike DCI contribution, the significance of this increase is much more evident at lower scan rates. For instance, PCI charge capacity contributions in the range of 34–73% and 62–90% were calculated for cycles 20 and 300, respectively, by increasing the scan rate from 0.2 to 3.0 mVs<sup>-1</sup>. Therefore, from these results it can be inferred that a considerable amount of the PF<sub>6</sub><sup>-</sup> anions, which are initially intercalated by the diffusion-controlled mechanism, becomes intercalated by the pseudo-capacitive mechanism with either cycling or by increasing the scan rate since the latter mechanism is kinetically more favored.

The contribution percentages of the two mechanisms to the PF<sub>6</sub><sup>-</sup> anion de-intercalation capacity of the graphite cathode for each scan rate in cycles 20, 50, 100, 200 and 300 are shown in Figure 5. As seen in Figure 5(a), the evolution with both cycling and scan rate of the DCDI contribution percentage to the electrode discharge capacity (PF<sub>6</sub><sup>-</sup> anion de-intercalation) is comparable to that of anion intercalation in Figure 4(a). However, this type of contribution to electrode capacity is much less significant in the de-intercalation than in the intercalation processes. For comparison, percentages of DCDI of 32%, 25%, 19% and 13% were calculated for the discharge at 0.2, 0.5, 1.0 and 3.0 mVs<sup>-1</sup>, respectively, against values of 66%, 58%, 50% and 38% of DCI for the charge. Therefore, regardless of cycling and scan rate, the graphite electrode discharge capacity is mainly due to a pseudo-capacitive de-intercalation

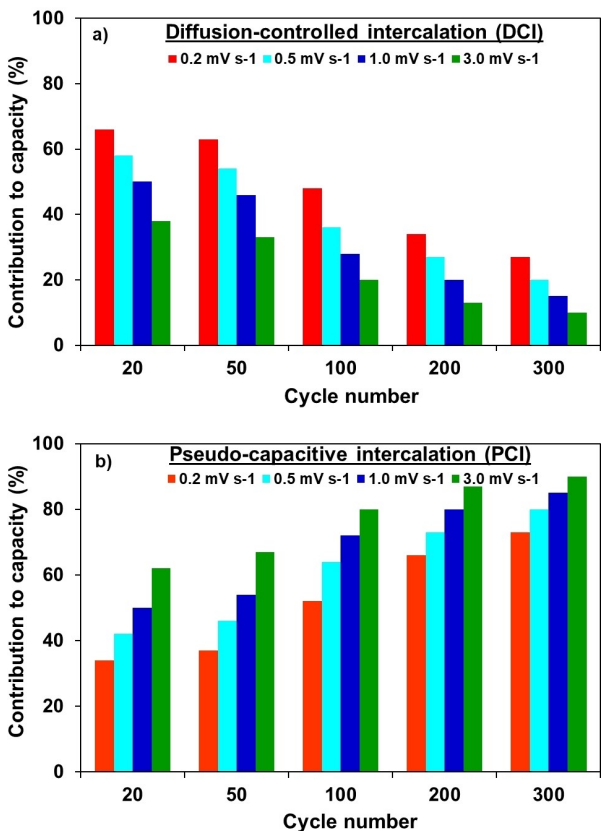


Figure 4. Contribution percentages of (a) diffusion-controlled and (b) pseudo-capacitive mechanisms to PF<sub>6</sub><sup>-</sup> anion intercalation in graphite (charge capacity) at scan rates from 0.2 to 3.0 mVs<sup>-1</sup> for cycles 20, 50, 100, 200 and 300.

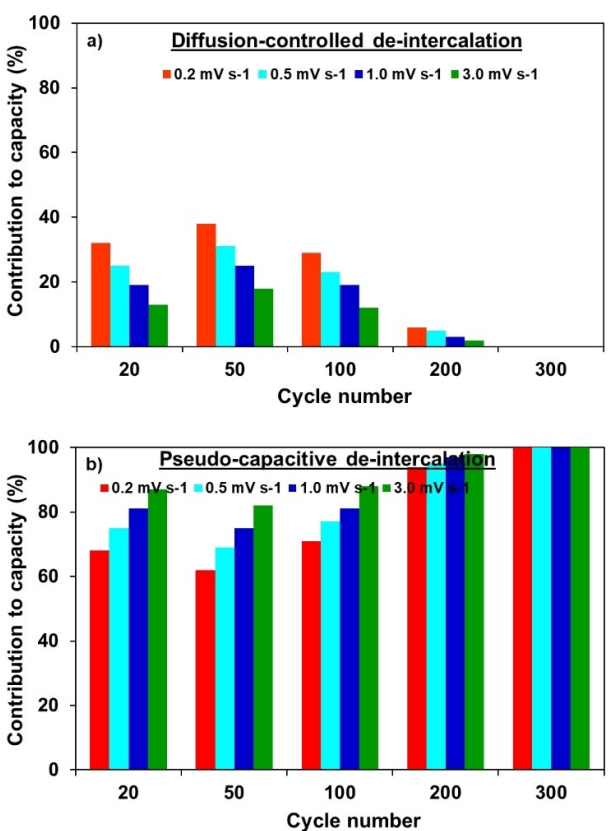


Figure 5. Contribution percentages of a) diffusion-controlled and b) pseudo-capacitive mechanisms to the PF<sub>6</sub><sup>-</sup> anion de-intercalation from graphite (discharge capacity) at scan rates from 0.2 to 3.0 mVs<sup>-1</sup> for cycles 20, 50, 100, 200 and 300.

mechanism (Figure 5b). In fact, the PCDI contribution is basically 100% from cycle 200 which agrees with the results of the qualitative analysis of anion intercalation/de-intercalation mechanisms from the *b* values (Figure 3).

In summary, from the qualitative and quantitative analysis of the CVs at different scan rates, it can be inferred that the pseudo-capacitive mechanism plays a predominant role in the electrochemical intercalation/de-intercalation of  $\text{PF}_6^-$  anions in graphite and this predominance becomes more evident with cycling. On the other hand, although initially there is a significant contribution to the measured current of the diffusion-controlled mechanism, particularly in the intercalation process at the highest potential, it tends to decrease with cycling, even disappearing in the discharge cycle 300 (Figures 3 and 5). Therefore, it seems that the continuous anion intercalation/de-intercalation may cause certain deterioration in the tri-dimensional ordered graphitic structure, which might prevent the diffusion-controlled intercalation, thus facilitating the pseudo-capacitive intercalation into the tunnels or layers of graphite accompanied by a faradaic charge-transfer without crystalline phase change.<sup>[29]</sup> In a previous work of our group we observed that the increase of the electrode material interlayer spacing, i.e., less ordered graphitic structure, promoted the pseudo-capacitive intercalation of  $\text{Na}^+$  ions.<sup>[36]</sup> To go further insight that issue, an exhaustive XRD-based structural analysis of the electrodes after cycling was carried out as described in the Experimental Section.

### Evolution of the cathode graphite-like structure during cycling

Figure 6 shows, as an example, the diffractograms in the  $22^\circ$ – $30^\circ$   $2\theta$  range of the graphite cathodes in discharge state after having been subjected to CV during 20 and 300 cycles at the different scan rates. For comparison, that of the fresh graphite cathode is included. First of all, a shift of the position of the (002) peak to lower  $2\theta$ , which is related to the decrease of the graphitic degree, is observed after cycling the graphite cathodes. In addition, this shift clearly increases with the number of cycles, being larger for the lower scan rates applied. In parallel, an increase of the full width at high medium (FWHM) of the (002) peak is also detected. Thus,  $2\theta$  values of  $26.33^\circ$  and  $26.25^\circ$  were determined for the graphite cathodes after 20 and 300 cycles, respectively, at the lowest  $0.2 \text{ mV s}^{-1}$  scan rate against a value of  $26.51^\circ$  for the fresh graphite cathode. To better compare these results, the structural parameters interlayer spacing,  $d_{002}$ , and the mean crystallite size along the *c* axis,  $L_c$ , as well as the degree of graphitization (DOG) of the graphite cathodes, both fresh and cycled, were calculated as described in the experimental section and they are given in Table 1. Independently of the scan rate applied, the degree of structural order of the graphite cathode decreases by cycling as shown by the increase of  $d_{002}$  and the decrease of  $L_c$ . Consequently, lower DOG values were calculated after cycling. As an example, the DOG and the  $L_c$  of the fresh graphite cathode decreases from 96% and 47 nm to the minimum values of 55% and 11 nm, respectively, after 300 cycles at a scan rate of  $0.2 \text{ mV s}^{-1}$ . These changes, which imply some deterioration of the graphitic

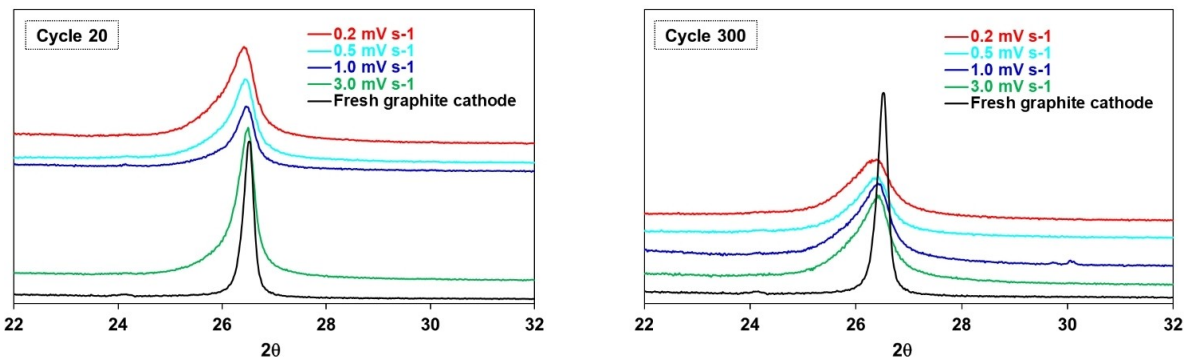


Figure 6. Ex-situ X-ray diffraction patterns of graphite cathodes: fresh and after 20 and 300 cycles at scan rates from  $0.2$  to  $3.0 \text{ mV s}^{-1}$ .

**Table 1.** Interlayer distance ( $d_{002}$ ) and crystallite size along *c*-axis ( $L_c$ ), and degree of graphitization (DOG) of fresh and cycled, at the different scan rates, graphite cathodes.

Fresh graphite cathode	Cycled graphite cathode							
	$0.2 [\text{mV s}^{-1}]$		$0.5 [\text{mV s}^{-1}]$		$1.0 [\text{mV s}^{-1}]$		$3.0 [\text{mV s}^{-1}]$	
	Cycle 20	Cycle 300						
$d_{002}$ [nm]	0.3358	0.3382	0.3393	0.3378	0.3388	0.3373	0.3387	0.3368
$L_c$ [nm]	47.0	13.0	9.1	14.9	11.0	17.7	11.0	22.4
DOG [%] <sup>[a]</sup>	96	67	55	72	61	78	62	84
[a] Degree of graphitization: $[(0.3440 - d_{002}) / (0.3440 - 0.3354)] \times 100$ .								

structure, already start from the initial cycles (after 20 cycles) and their significance is highly influenced by the scan rate. In fact, after 20 cycles, there is a trend of the DOG to decrease as the scan rate decreases, i.e., the graphite cathode structural deterioration is higher for lower scan rates. As seen in Table 1, at this cycling point, DOG values of 84%, 78%, 72% and 67% were calculated for the graphite cathodes at 3.0, 1.0, 0.5 and 0.2 mVs<sup>-1</sup>, respectively, and the corresponding crystallite sizes,  $L_c$ , were ~22, ~18, ~15, and ~13 nm. These results, which confirm the above-mentioned hypothesis of the graphite cathode structural deterioration during cycling, provide an explanation for the predominance of the PCI/PCDI processes for the intercalation/de-intercalation of the PF<sub>6</sub><sup>-</sup> anion into/from the graphite cathode, particular after the initial cycles and at the lowest scan rates in which this deterioration was found to be higher (Figures 2–5).

## Conclusions

The intercalation/de-intercalation of the PF<sub>6</sub><sup>-</sup> anions, from sodium salt-based electrolytes, in a graphite cathode of dual-ion batteries occurs through a combination of diffusion-controlled and pseudocapacitive mechanisms. Initially, the contribution of the diffusion-controlled mechanism is significant, specifically at the highest voltage studied around 4.9 V and at the lowest scan rates applied, which agrees with the slow kinetic nature of this mechanism and its usual prevalence in the intercalation/de-intercalation of ions in carbon materials with a high degree of development of the graphite-type structure. However, the continuous anion intercalation/de-intercalation causes certain deterioration of the graphite tri-dimensional structural order, even from the initial cycles, as it was demonstrated by the evolution of the graphite crystalline parameters, interlayer spacing,  $d_{002}$ , and crystallite size,  $L_c$ . This deterioration hinders the diffusion-controlled intercalation/de-intercalation of the anions and, as a consequence, the pseudocapacitive intercalation/de-intercalation becomes the main mechanism along the cycling. Therefore, since graphite electrodes are capable of intercalating PF<sub>6</sub><sup>-</sup> anions at high voltages through a capacitive mechanism, with its consequent rapid kinetics, these electrodes are excellent candidates for using as cathodes in high power sodium dual-ion batteries, in which, kinetically fast mechanisms are required.

## Experimental Section

### Materials: source and characteristics

A commercial synthetic graphite (SG) was selected as cathode active material (KS6, Imerys [www.imerys.com](http://www.imerys.com)). The crystalline parameters interlayer spacing,  $d_{002}$ , and the mean crystallite size along the perpendicular c,  $L_c$ , plane of SG were calculated from the X-ray diffractograms, which were recorded in a Bruker D8 powder diffractometer with a Göbel mirror configuration, as described in a previous work.<sup>[37]</sup> Values of  $d_{002}$  and  $L_c$  of approximately 0.3360 nm and 37 nm, respectively, were determined for this graphite. A

degree of graphitization (DOG) of 93% was calculated from the following equation: DOG (%) = [(0.3440 -  $d_{002}$ ) / (0.3440 - 0.3354)] × 100.

The BET surface area ( $S_{BET}$ ) of SG, calculated by applying the Brunauer-Emmett-Teller (BET) method to its nitrogen adsorption-desorption isotherm, was 20 m<sup>2</sup> g<sup>-1</sup>. Isotherm was obtained at -196 °C after being degassed overnight at 250 °C in a Micromeritics ASAP 2410 system. A cross sectional area of the nitrogen-adsorbed molecule of 0.162 nm<sup>2</sup> was considered for this calculation.

For the preparation of the SG-based electrodes, sodium carboxymethylcellulosa (NaCMC, Mw ~700.000, Sigma-Aldrich) and carbon black (Super C65, Imerys) were used as binder and electric conductive additive, respectively. Sodium hexafluorophosphate (NaPF<sub>6</sub> > 99% purity, Alfa-Aesar) salt and ethylene carbonate (EC, 99.0% purity, Merck) and ethyl methyl carbonate (EMC, 99.9% purity, Sigma-Aldrich) solvents were used to prepare the electrolyte.

### Electrolyte and work electrode preparation, cell assembly, and electrochemical measurements

A solution of 2.0 M NaPF<sub>6</sub> dissolved in 1:1 mixture (w:w) of EC and EMC, denoted as 2MNaPF<sub>6</sub>/EC:EMC, was used as electrolyte. The preparation of the electrolyte involved the following steps: (i) the salt was vacuum dried at 80 °C for 16 hours; (ii) the solvents were mixed in the indicated proportion and stored with 4 Å zeolite type (3–5 mm beads from Alfa-Aesar) to eliminate possible traces of moisture; (iii) finally the salt and the solvents, previously filtered, were mixed and magnetically stirred for 24 hours at ambient temperature. Both (ii) and (iii) steps were carried out inside a glove box (MBraun) under an Ar atmosphere with H<sub>2</sub>O and O<sub>2</sub> contents < 0.1 ppm.

The composition of the working electrodes (WE) was 70 wt.% of SG, 20 wt.% of NaCMC binder and 10 wt.% of Super C65 conductive additive. WE preparation procedure was as follows: (i) NaCMC was dissolved in de-ionized water by mechanical stirring (IKA Overhead Stirrer Eurostar 20) at 2000 rpm during 1 h (~1.0 wt.% solution), (ii) Super C65 was mixed with NaCMC solution maintaining the stirring at 1000 rpm for 10 minutes to achieve a homogeneous dispersion, (iii) SG was then added gently to form an slurry which was stirred at 4000 rpm for 1 hour to ensure the absence of agglomerates and an excellent dispersion, (iv) the slurry was spread over an aluminum foil (99.3 wt.% purity, 20 µm thickness, Hohsen Corporation, Japan) by tape-casting using a doctor blade with a gap of 350 µm pushed by a motorized/authomatic film applicator (Elcometer 4340) provided with a perforated heated vacuum table, (v) the aluminum electrode tape was kept on the applicator table under vacuum at 80 °C for 1 hour, (vi) 12 mm diameter electrodes were cut using a manual punching machine and (vii) the electrodes were dried for 2 h at 120 °C under vacuum in a Büchi oven and finally stored in the glove box. The SG-based electrodes load (referred to the active SG material) calculated by weight difference was in the range of 1.25–1.50 mg cm<sup>-2</sup>.

Two-electrode (working, WE, and counter, CE, electrodes) Swagelok-type cells were used. A 12 mm-diameter metallic sodium (dry Na > 99.99 wt.% purity from Merck/Sigma Aldrich) disc was the CE. Two 12 mm-diameter micro-fiber glass (Whatman GF/A) discs soaked with 160 µL of the electrolyte were place between WE and CE as separator. The assembly of the cells was carried out inside the glove box, being the initial potential in the 2.5–3.0 V vs. Na/Na<sup>+</sup> range. In this work, since the potential is always referred to the Na/Na<sup>+</sup> redox couple, the terms potential and voltage are used interchangeably. Cyclic voltammetry (CV) at 0.2, 0.5, 1.0 and

3.0 mVs<sup>-1</sup> scan rates of the cells were conducted in a Biologic battery testing system (BCS 810) for 300 cycles in the 2.9–5.0 V voltage range.

### Ex-situ XRD of graphite-based cathodes after cycling

The graphite-like structure of the WEs after 20 and 300 cyclic voltammetries at the different scan rates was studied by ex-situ XRD in the discharge state. For this, once the CV was finished, the cell was disassembled inside the glove box and the WE was stored in a vessel with EC:EMC (1:1, w:w) for ~48 hours. Subsequently, the electrode was transferred to another vessel without solvent and it was dried in the glove box at room temperature for at least 48 hours. Then, the XRD measurements were also carried out in the Bruker D8 powder diffractometer as indicated.<sup>[35]</sup> In this case, scans were made in four different  $2\theta$  intervals (5–90°, 18–42°, 15–35° and 22–30°) with a time and size step of 3 s and 0.02°, respectively. For comparison, a fresh uncycled WE was also analyzed following the same procedure. The interlayer spacing,  $d_{002}$ , and mean crystallite sizes along the c axis,  $L_c$ , were calculated from the diffractograms with typical standard errors of <0.05% and <7.00%, respectively. In addition, the DOG was determined as described above.

### Acknowledgements

This research was supported by MCIN/AEI/10.13039/501100011033 and the European Union NextGenerationEU/PRTR (Project PID2020-113001RB-I00) and Principado de Asturias (Project IDI/2021/50921). I. Cameán thanks the funding from Fundación General CSIC (Programa ComFuturo, II Edition) to develop the work.

### Conflict of Interests

The authors declare no conflict of interest.

### Data Availability Statement

The data that support the findings of this study are available from the corresponding author upon reasonable request.

**Keywords:** sodium dual-ion battery · graphite cathode · PF<sub>6</sub><sup>-</sup> anion · diffusion-controlled intercalation · pseudocapacitive intercalation

- [1] T. Placke, A. Heckmann, R. Schmuck, P. Meister, K. Beltrop, M. Winter, *Joule* **2018**, *2*, 2528.
- [2] M. Wang, Y. Tang, *Adv. Energy Mater.* **2018**, *8*, 1703320.
- [3] Z. Hu, Q. Liu, K. Zhang, L. Zhou, L. Li, M. Che, Z. Tao, Y.-M. Kang, L. Mai, S.-L Chou, J. Chen, S.-X. Dou, *Appl. Mater. Interf.* **2018**, *10*, 35978.

- [4] B. Heidrich, A. Heckmann, K. Beltrop, M. Winter, T. Placke, *Energy Storage Mater.* **2019**, *21*, 414.
- [5] Z. Guo, Z. Xu, F. Xie, J. Feng, M. Titirici, *Adv. Energy Sustainability Res.* **2021**, *2*, 2100074.
- [6] P. Meister, O. Fromm, S. Rothenmel, J. Kasnatscheew, M. Winter, T. Placke, *Electrochim. Acta* **2017**, *228*, 18.
- [7] J. A. Read, A. V. Cresce, M. H. Ervin, K. Xu, *Energy Environ. Sci.* **2014**, *7*, 617.
- [8] X. Jiang, L. Luo, F. Zhong, X. Feng, W. Chen, X. Ai, H. Yang, Y. Cao, *ChemElectroChem* **2019**, *6*, 261.
- [9] L. Fan, Q. Liu, S. Chen, Z. Xu, B. Lu, *Adv. Energy Mater.* **2017**, *7*, 1602778.
- [10] S. Aladinli, F. Bordet, K. Ahlbrecht, J. Tübke, M. Holzapfel, *Electrochim. Acta* **2017**, *231*, 468.
- [11] Z. Guo, G. Cheng, Z. Xu, F. Xie, Y.-S. Hu, C. Mattevi, M.-M. Titirici, M. C. Ribadeneyra, *ChemSusChem* **2022**, *16*, e202201583.
- [12] A. Heckmann, J. Thienenkamp, K. Beltrop, M. Winter, G. Brunklaus, T. Placke, *Electrochim. Acta* **2018**, *260*, 514.
- [13] Z. Liang, D. Gong, J. Shang, H. Cheng, X. Pu, D. Wang, L. Zhang, C. Wang, C.-S. Lee, Y. Tang, *Energy Storage Mater.* **2022**, *53*, 331.
- [14] X. Zhang, L. Zhang, W. Zhang, S. Xu, Y. Tang, *J. Power Sources* **2022**, *518*, 230741.
- [15] I. Cameán, N. Cuesta, A. B. García, *Electrochim. Acta* **2021**, *384*, 138360.
- [16] I. Cameán, B. Lobato, N. Cuesta, A. B. García, *Electrochim. Commun.* **2021**, *128*, 107075.
- [17] W. Wang, H. Huang, B. Wang, C. Qian, P. Li, J. Zhou, Z. Liang, C. Yang, S. Guo, *Sci. Bull.* **2019**, *64*, 1634.
- [18] M. Sheng, F. Zhang, B. Ji, X. Tong, Y. Tang, *Adv. Energy Mater.* **2017**, *7*, 1601963.
- [19] F. Wang, Z. Liu, P. Zhang, H. Li, W. Sheng, T. Zhang, R. Jordan, Y. Wu, X. Zhuang, X. Feng, *Small* **2017**, *13*, 1702449.
- [20] S. Dong, Y. Xu, L. Wu, H. Dou, X. Zhang, *Energy Storage Mater.* **2018**, *11*, 8.
- [21] S. Chen, J. Wang, L. Fan, R. Ma, E. Zhang, Q. Liu, B. Lu, *Adv. Energy Mater.* **2018**, *8*, 1800140.
- [22] X. Qi, J. Mao, *J. Phys. Chem. Lett.* **2021**, *12*, 5430.
- [23] I. Caméan, B. Lobato, N. Rey-Raab, L. dos Santos-Gómez, S. Flores-López, A. Arenillas, A. B. García, *ChemElectroChem* **2023**, *10*, e202201069.
- [24] F. Bordet, K. Ahlbrecht, J. Tübke, J. Ufheil, T. Hoes, M. Oetken, M. Holzapfel, *Electrochim. Acta* **2015**, *174*, 1317.
- [25] S. Aladinli, F. Bordet, K. Ahlbrecht, J. Tübke, M. Holzapfel, *Electrochim. Acta* **2017**, *228*, 503.
- [26] G. Wang, M. Yu, J. Wang, D. Li, D. Tan, M. Löffler, X. Zhuang, K. Müllen, X. Feng, *Adv. Mater.* **2018**, *30*, 1800533.
- [27] S. Trasatti, G. Buzzanca, *J. Electroanal. Chem. Interfacial Electrochem.* **1971**, *29*, 1.
- [28] B. E. Conway, *Electrochemical Supercapacitors: Scientific Fundamentals and Technological Applications*, Kluwer-Academic **1999**.
- [29] V. Augustyn, P. Simon, B. Dunn, *Energy Environ. Sci.* **2014**, *7*, 1597.
- [30] T. Brezesinski, J. Wang, S. H. Tolbert, B. Dunn, *Nat. Mater.* **2010**, *9*, 146.
- [31] Z. Zhu, F. Cheng, Z. Hu, Z. Niu, J. Chen, *J. Power Sources* **2015**, *293*, 626.
- [32] H. Lindstrom, S. Sodergren, A. Solbrand, H. Rensmo, J. Hjelm, A. Hagfeldt, S. E. Lindquist, *J. Phys. Chem. B* **1997**, *101*, 7717.
- [33] J. Wang, J. Pollex, J. Lin, B. Dunn, *J. Phys. Chem. C* **2007**, *111*, 14925.
- [34] Y. Wang, Y. Zhang, Q. Duan, P. K. Lee, S. Wang, D. Y. W. Yu, *J. Power Sources* **2020**, *471*, 228466.
- [35] H. Fan, L. Qi, M. Yoshio, H. Wang, *Solid State Ion.* **2017**, *304*, 107.
- [36] I. Cameán, J. Rodríguez-García, A. B. García, *J. Electrochem. Soc.* **2019**, *166*, A403.
- [37] I. Cameán, A. B. García, *J. Power Sources* **2011**, *196*, 4816.

Manuscript received: October 31, 2023

Revised manuscript received: November 21, 2023

Accepted manuscript online: November 21, 2023

Version of record online: December 13, 2023